Inorganic Chemistry

Article

pubs.acs.org/IC

μ-O Bridged Mn_{10} Assemblies with Open O_6 Sites for Binding Extra Guests: Structural, Magnetic, and Surface Studies

Muhammad U. Anwar,[†] Louise N. Dawe,[†] Mohammad S. Alam,[‡] and Laurence K. Thompson*,[†]

[†]Department of Chemistry, Memorial University, St. John's, NL, A1B 3X7, Canada

[‡]Department of Physics, Faculty of Science, University of Dhaka, Dhaka-1000, Bangladesh

Supporting Information

ABSTRACT: High nuclearity $[Mn_{10}M_2]$ clusters have been achieved through a self-assembly approach where multiple coordinating functional groups are incorporated into one ligand. When the hydrazone group appended with an oxime function as a reactive intermediate is used, the attachment of a vanillin subunit creates a ligand (L4) with three coordinating groups, which in their own right lead to cluster assemblies. The trifunctional ligand L4 produces a series of self-assembled, mixed oxidation state (Mn(II)/Mn(III)) $Mn_{10}M_2$ based clusters with an overall linear structure comprising two connected pentanuclear Mn_5 halves, which bind alkali metal cations (M = Li, Na, K, Rb, Cs) and H_3O^+ in the vanillin (O_6) end pockets, created by the assembly of three ligands around each Mn_5 subunit. Antiferromagnetic exchange dominates the spin coupling in the Mn_{10} complexes, and surface studies on highly oriented pyrolytic graphite (HOPG) clearly show the arrangement of metal ions (Mn, Cs) in the $Mn_{10}Cs_2$ linear cluster assembly.

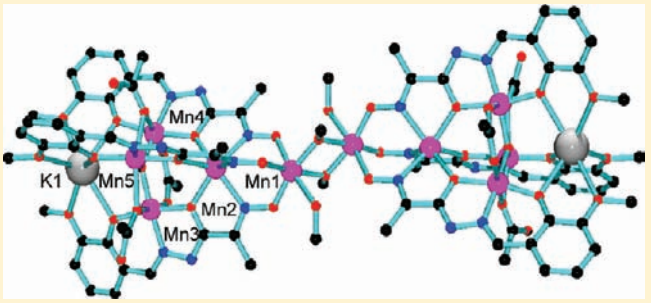

INTRODUCTION

Ligand based approaches to self-organized and possibly predictable cluster assemblies rely on incorporating specific functional donor groups, arranged in a particular way within the ligand, such that predetermined complex architectures may be synthesized through self-assembly. Simple substituted polytopic hydrazones have served this function well, and have produced many $[n \times n]$ $(n = 2-5)$ μ-O bridged square grid based complexes with first row transition metal ions.[1−3] Typical ligands involve pendant pyridine and related heterocyclic groups (see Chart 1 for typical ditopic, for example, poap, and tritopic, for example, 2poap and related ligand examples) with the hydrazone "O" group providing a bridging focus between metal ions. The key design element involves presenting the donor atoms in such a way, through preferred tautomeric ligand conformations, that five-membered chelate rings are formed on coordination, and that the sequence of these rings is linear. Oxime groups have a propensity to form aggregated metal triangles through NO, and often adventitious μ_3-O bridging. Ligands L1-L3 have been elaborated with oxime groups as part of the hydrazone portion, with the specific intention of testing the possibility of aggregation of grids through secondary self-assembly events. With L1 three ligands have been shown to assemble around a $[Cu_3(\mu_3\text{-O})(\mu\text{-NO})_3]$ triangular cluster, formed through the combination of three oxime ends of three ligands, to create a novel $Cu(II)_6$ cluster, with the other ends of the three ligands binding to three additional Cu(II) ions in a spiral fashion through μ-NN diazine bridges.[4] This illustrates the partial success of the approach, but shows that alternative hydrazone bridging modes, involving different ligand tautomers are also possible.

O-vanillin has been explored as a ligand in its own right, and also as a functional group in expanded ligands, and its lanthanide chemistry has been a major recent focus, in part because some polynuclear Dy(III) complexes, which have resulted, exhibit Single Molecule Magnet (SMM) behavior at low temperature.[5−9] The phenolic oxygen of the *o*-vanillin group provides a bridging focus, and is in part responsible for cluster formation. The incorporation of an *o*-vanillin group on an oxime functionalized hydrazone, as in L4 (Chart 1), provides multiple coordination potential with the possibility of oxime bridging in addition to bridging through both hydrazone and phenolic oxygen atoms. A preliminary report shows that L4 forms a unique, but unexpected deca-manganese dimeric cluster, $[Cs_2Mn_{10}(L4\text{-}3H)_6(O)_2(CH_3O)_4(CH_3COO)_6(CH_3OH)_2]\cdot 12H_2O$ (**1**),[10] with two methoxide bridged Mn_5 subunits involving both μ-O and μ-NO bridges, and a mixture of Mn(III) and Mn(II) sites. Two groups of three *o*-vanillin subunits each from three ligands are bound around each Mn_5 subunit in a trigonal fashion and meet at both complex ends, providing a fortuitous terminal assembly of six oxygen atoms, ideally suited for the incorporation of the two Cs^+ ions. This complex exhibits intramolecular antiferromagnetic exchange.[10]

The present report describes other related $Mn_{10}M_2$ complexes in this series (M = Li, Na, K, Rb, H_3O^+). Structural and magnetic properties on the complexes are reported and

Received: February 14, 2012
Published: March 29, 2012

Chart 1

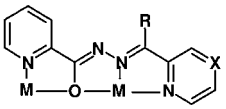

poap (R=NH_2,X=CH),
poapz (R=NH_2,X=N)

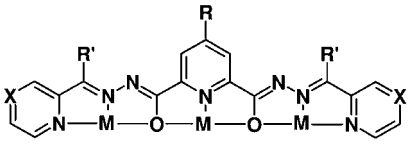

2poap(R=H,R'=NH_2,X=CH),Cl2poap(R=Cl,R'=NH_2,X=CH),
2pomp(R=H,R'=CH_3,X=CH),Cl2pomp(R=Cl,R'=CH_3,X=CH),
2poapz(R=H,R'=NH_2,X=N),2popp(R=H,R'=Ph,X=CH)

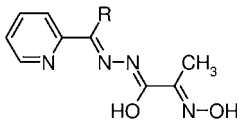

L1 (R=H), L2 (R=CH_3), L3 (R=NH_2)

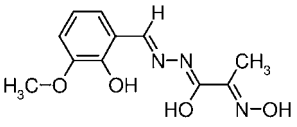

L4

discussed, and in addition surface studies on **1** deposited on highly oriented pyrolytic graphite (HOPG) are highlighted.

EXPERIMENTAL SECTION

EA, IR, and MS spectroscopy. Elemental analyses were carried out by Canadian Microanalytical Service, Delta, BC, Canada. Infrared spectra were obtained as Nujol mulls on a Bruker Tensor 27 instrument.

Synthesis of Ligand. L4 was synthesized according to the reported procedure.[10]

Synthesis of Complexes. *Synthesis of* $[Mn_{10}(L4\text{-}3H)_6(O)_2(H_3O)_2(CH_3O)_2(CH_3COO)_6(CH_3OH)_2](H_2O)_{12}$ (**2**). *o*-Vanillin (0.070 g, 0.46 mmol), (2-(hydroxyimino)-propanehydrazone[10] (0.060 g, 0.51 mmol), and $Mn(CH_3COO)_2{\cdot}4H_2O$ (0.20 g, 0.80 mmol) were stirred together in MeOH for 2−3 min, followed by addition of 10 drops of triethyl amine. After stirring for 2.5 h at room temperature, the solution was filtered, and the filtrate was layered with ethyl ether. Dark brown crystals appeared in a few days (Yield: 0.020 g, 25%). Selected IR data (Nujol, cm^{-1}): 3352 (ν_{OH}), 1714 (ν_{CO}), 1609 (ν_{CO}), 1561 (ν_{CN}), 1296, 1215, 1170, 1122, 1083, 1024, 968, 924, 726, Elemental Analysis (%): Calcd for $Mn_{10}(C_{11}H_{10}N_3O_4)_6(O)_2(H_3O)_2(CH_3O)_2(CH_3COO)_6(CH_3OH)_2(H_2O)_{12}$: C, 35.12 H, 4.31; N, 8.99. Found: C, 34.78; H, 3.83; N, 9.49.

Synthesis of $[Mn_{10}(L4\text{-}3H)_6(O)_2(CH_3O)_4(CH_3COO)_4Li_2(LiOH)_2(CH_3OH)_2]$ (**3**). Ligand L4 (0.050 g, 0.19 mmol) and $Mn(CH_3COO)_2{\cdot}4H_2O$ (0.20 g, 0.80 mmol) were stirred together in MeOH for 2−3 min, followed by addition of 20 drops of 0.5 M aqueous solution of LiOH. After stirring for 30 min at room temperature the solution was filtered, and the filtrate was layered with ethyl ether. Dark brown crystals appeared in a week (Yield: 0.063 g, 70%). Selected IR data (Nujol, cm^{-1}): 3466 (ν_{OH}), 1714 (ν_{CO}), 1606 (ν_{CO}), 1555 (ν_{CN}), 1287, 1214, 1172, 1122, 1082, 1030, 967, 921, 728. Elemental Analysis (%): Calcd for $Mn_{10}(C_{11}H_{10}N_3O_4)_6(O)_2(CH_3O)_4(CH_3COO)_4$ $Li_2(LiOH)_2(CH_3OH)_2$: C, 37.59; H, 3.75; N, 9.86. Found: C, 38.09; H, 4.05; N, 9.67.

Synthesis of **4**−**6**. Compounds **4**−**6** were synthesized following the same procedure as for **3**, using the appropriate alkali metal hydroxide solution. $[Mn_{10}(L4\text{-}3H)_6(O)_2(CH_3O)_2(CH_3OH)_2$ $(CH_3COO)_6Na_2](H_2O)_7$ (**4**); dark brown crystals (Yield 28%). Selected IR data (Nujol, cm^{-1}): 3400 (ν_{OH}), 1713 (ν_{CO}), 1636 (ν_{CO}), 1602 (ν_{CN}), 1286, 1248, 1211, 1169, 1121, 1087, 1015, 965, 917, 729. Elemental Analysis (%): Calcd for $Mn_{10}(C_{11}H_{10}N_3O_4)_6(O)_2(CH_3O)_2$ $(CH_3OH)_2(CH_3COO)_6Na_2(H_2O)_7$: C, 36.14; H, 3.89; N, 9.26. Found: C, 35.93; H, 3.03; N, 9.61. $[Mn_{10}(L4\text{-}3H)_6(O)_2(CH_3O)_2(CH_3OH)_2(CH_3COO)_6K_2](H_2O)_6$ (**5**); dark brown crystals (Yield 62%). Selected IR data (Nujol, cm^{-1}): 3350 (ν_{OH}), 1710 (ν_{CO}), 1607 (ν_{CO}), 1559 (ν_{CN}), 1213, 1169, 1122, 1024, 921, 726. Elemental Analysis (%): Calcd for $Mn_{10}(C_{11}H_{10}N_3O_4)_6(O)_2$ $(CH_3O)_2(CH_3OH)_2$ $(CH_3COO)_6K_2(H_2O)_6$: C, 36.01; H, 3.76; N, 9.22. Found: C, 35.88; H, 3.08; N, 9.43. $[Mn_{10}(L4\text{-}3H)_6(O)_2(CH_3O)_2(CH_3OH)_2(CH_3COO)_6Rb_2[(H_2O)_7$ (**6**); dark brown crystals (Yield 37%). Selected IR data (Nujol, cm^{-1}): 3350 (ν_{OH}), 1715 (ν_{CO}), 1609 (ν_{CO}), 1561 (ν_{CN}), 1286, 1249, 1213, 1169, 1123, 1084, 1016, 966, 920, 728. Elemental Analysis (%): Calcd for $Mn_{10}(C_{11}H_{10}N_3O_4)_6(O)_2(CH_3O)_2(CH_3OH)_2(CH_3COO)_6Rb_2(H_2O)_7$: C, 34.59; H, 3.65; N, 8.86. Found: C, 34.25; H, 3.06; N, 9.11.

Single Crystal X-ray Diffraction Studies. Crystals of **2**−**6** were mounted on low temperature diffraction loops and measured on a Rigaku Saturn CCD area detector with graphite monochromated Mo−Kα radiation. Structures were solved by direct methods[11] and expanded using Fourier techniques.[12] Neutral atom scattering factors were taken from Cromer and Waber.[13] Anomalous dispersion effects were included in F_{calc};[14] the values for $\Delta f'$ and $\Delta f''$ were those of Creagh and McAuley.[15] The values for the mass attenuation coefficients are those of Creagh and Hubbell.[16] All calculations were performed using CrystalStructure[17,18] and Platon[19] crystallographic software packages, except for refinement, which was performed using SHELXL-97.[11] Non-hydrogen atoms were refined anisotropically, while hydrogen atoms were introduced in calculated positions and refined on a riding model, unless otherwise indicated. CCDC nos. 814529 (for **1**) and 866472−866476 (for **2**−**6**).

For **2** and **5**, protons for lattice solvent water and methanol molecules that could not be located in difference map positions were omitted from the model; however, these H-atoms were included in the formula for the calculation of intensive properties. The occupancies of the two disordered acetate parts were refined for **2**, as well as for disordered lattice methanol molecules for 5, with the application of similarity restraints in both cases. For **3**, two protons are missing from the asymmetric unit; one from the LiOH moiety and one from the OH of a bridging methanol molecule. Li2−O21 and Li2A-O21A are partial occupancy LiOH moieties; their occupancies were refined and sum to one. The occupancies of both lattice solvent diethyl ether molecules were also refined, and summed to one with the application of similarity and distance restraints.

The Platon[19] SQUEEZE procedure was applied to **4** and **6**. For **4**, 523 electrons per unit cell were recovered in one void (total volume 1745 Å^3); that is 261.5 electrons per formula unit. Lattice solvent methanol molecules (18 electrons/CH_3OH) were present, and the electrons recovered by SQUEEZE have been assigned as 14 methanol molecules per formula unit. Further, one proton is missing from the asymmetric unit, from the OH of a bridging methanol molecule. For **6**, 274 electrons per unit cell were recovered in one void (total volume 1872 Å^3); that is, 137 electrons per formula unit. Lattice solvent water molecules (10 electrons/H_2O) were present, and the electrons recovered by SQUEEZE have been assigned as 13 water molecules per formula unit. The Rb atom was disordered over two sites. This was modeled as two parts, with refined occupancies (Rb1 = 0.422(10), Rb2 = 0.578(10)). The methanolic proton H23 was located from difference Fourier maps and was refined with distance and angle restraints. For both **4** and **6**, molecules omitted by SQUEEZE have been included in the formula for the calculation of intensive properties.

STM Experiments. All measurements were carried out with a home-built low drift STM (scanning tunneling microscopy) head equipped with control electronics under ambient conditions. For the high resolution STM studies a HOPG surface, freshly cleaved with adhesive tape, was used. Before sample imaging, the substrate was imaged by STM, using the images of the graphite lattice to confirm the resolution of the tip, and calibrate the spatial separation of the STM

dx.doi.org/10.1021/ic3003355 | Inorg. Chem. 2012, 51, 11241−11250

Table 1. Crystallographic Details for Complexes 2−6

	2	3	4	5	6
chemical formula	$C_{90.5}H_{121}Mn_{10}N_{18}O_{47}$	$C_{88}H_{114}Li_2Mn_{10}N_{18}O_{44}$	$C_{96}H_{148}Mn_{10}Na_2O_{56}$	$C_{93}H_{124}K_2Mn_{10}N_{18}O_{47}$	$C_{82}H_{118}Mn_{10}N_{18}O_{55}Rb_2$
M	2762.42	2705.11	3045.67	2873.67	2956.24
T(K)	153(2)	163(2)	163(2)	163(2)	153(2)
crystal system	monoclinic	monoclinic	monoclinic	monoclinic	monoclinic
space group	$P2_1/c$ (#14)	$P2_1/c$ (#14)	$P2_1/c$ (#14)	$P2_1/c$ (#14)	$P2_1/c$ (#14)
a (Å)	20.902(5)	11.464(3)	21.297(9)	20.693(13)	21.159(15)
b (Å)	16.791(4)	29.230(7)	16.518(7)	16.5209(10)	16.950(11)
c (Å)	17.681(4)	18.674(4)	17.945(8)	17.835(11)	17.908(11)
α (deg)	90.00	90.00	90.00	90.00	90.00
β (deg)	92.793(5)	93.967(3)	95.885(4)	93.557(7)	95.061(9)
γ (deg)	90.00	90.00	90.00	90.00	90.00
V (Å^3)	6198(2)	6243(3)	6250(5)	6085(5)	6398(7)
Z	2	2	2	2	2
D_{calc} (g/cm^3)	1.480	1.439	1.618		1.535
μ(MoKα) (cm^{-1})	10.71	10.59	10.82	11.61	17.98
reflections total	75460	55522	77840	74244	11264
reflections unique ($I > 2.00\sigma(I)$)	10837	11835	10616	12590	8105
R_{int}	0.0495	0.0348	0.0687	0.0926	0.0612
R_1 ($I > 2.00\sigma(I)$)	0.0846	0.0680	0.0802	0.0936	0.0984
wR_2 (all reflections)	0.2418	0.2495	0.2414	0.26644	0.3137

Table 2. Important Dimensions for 2−6[a]

complex (M)	Mn−O_{hyd}−Mn (deg)	Mn−O_{tr}−Mn (deg)	Mn−O_{Ac}−Mn (deg)	Mn_3 bridges
2 (H_3O^+)	127.1−130.9	107.3−125.9 (Sum 353.2)	92.3−92.5	1xμ_2-1,1-acetate
				1xμ_2-1,3-acetate
				1 disordered acetate
3 (Li^+)	125.5−132.0	99.3−126.6 (Sum 351.7)	94.8	2xμ_2-1,3-acetate
				1xμ-OMe
4 (Na^+)	128.5−130.3	112.2−129.2 (Sum 354.9)	88.7−89.6	2xμ_2-1,1-acetate
				1xμ_2-1,3-acetate
5 (K^+)	129.4−130.7	112.2−126.3 (Sum 352.8)	90.2−91.3	2xμ_2-1,1-acetate
				1xμ_2-1,3-acetate
6 (Rb^+)	129.4−131.2	110.6−128.4 (Sum 352.5)	89.3−94.0	2xμ_2-1,1-acetate
				1xμ_2-1,3-acetate

[a]M = Cs^+ (**1**) 2 × μ_2-1,3-acetate, 1 × μ-OMe.[10]

images. After imaging the graphite surface successfully a droplet of complex (**1**) in CH_3OH was taken (10^{-8} M) and allowed to run down the graphite surface and evaporate to deposit the sample. Typically, tunneling currents between 5 and 40 pA were employed. The bias voltage was ±100 mV to ±200 mV. The scan frequency was varied between 1 and 3 Hz. Resolution was 256 × 256 points for topography, and 128 × 128 in the CITS measurements. CITS measurements were performed simultaneously with topographic imaging, using the interrupted feedback loop technique.[20] This was achieved by opening the feedback loop at a fixed separation of tip and sample, and ramping the bias voltage over the range of interest. The scan range of voltages was typically from −0.8 V to +0.8 V relative to the tip potential for approximately 100 discrete voltage steps. Pt−Ir (90/10) tips were used, mechanically cut from wires with a diameter of 0.25 mm. Figures.13 and 14 were produced using the program WSxM.[21]

RESULTS AND DISCUSSION

Description of Structures. *$[Mn_{10}(L4\text{-}3H)_6(O)_2(H_3O)_2(CH_3COO)_6(CH_3O)_2(CH_3OH)_2]$ $(H_2O)_{2.5}(CH_3OH)_{0.5}(C_4H_{10}O)_2$ (**2**).* Crystallographic details for **2** are given in Table 1, and important bond distances and angles in Supporting Information, Table S1. A summary of key dimensions is given in Table 2. The structure of the deca-manganese cluster is shown in Figure 1, with an abbreviated structure showing just the immediate donor atoms

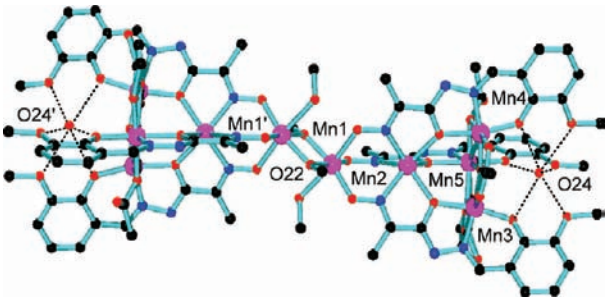

Figure 1.

shown in Figure 2. The structure is composed of two penta-manganese halves connected via two methoxide bridges through inversion symmetry (Mn1−O22 1.954(4) Å, Mn1−O22′ 1.944(4) Å). Each half involves three trigonally disposed ligands wrapped around a group of five manganese centers in a cluster comprising a pyramidal group of four (Mn2−Mn5) metals connected via Mn2 to a single metal ion Mn1 through three oxime (NO) bridges (Figure 3). Within the Mn_4 pyramid Mn3, Mn4, and Mn5 are arranged in a triangle and bridged through a μ_3-O linkage. The short Mn−O13 distances (Mn3; 1.888, Mn4; 1.895; Mn5; 1.935 Å)

dx.doi.org/10.1021/ic3003355 | Inorg. Chem. 2012, 51, 11241−11250

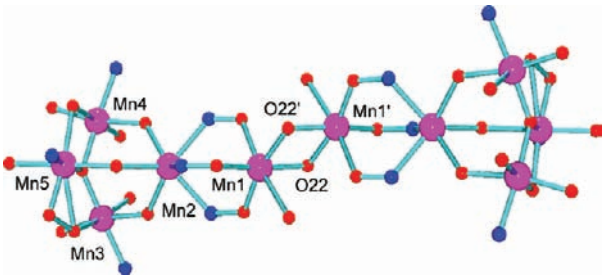

Figure 2.

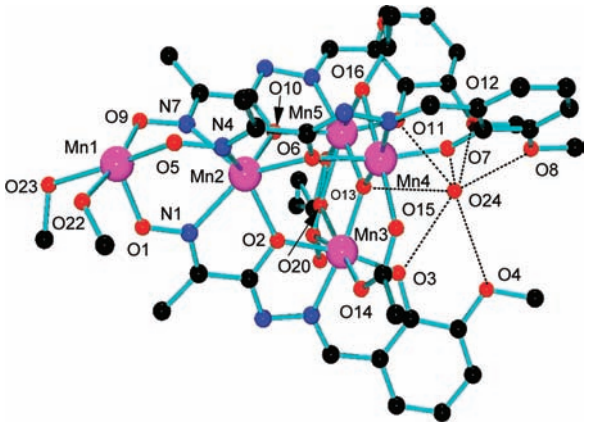

Figure 3.

indicate that O13 is a bridging oxide ion. Mn−O−Mn angles fall in the range 107.3−125.9°, with an angle sum of 353.2°, indicating a slight pyramidal distortion at O13. Each of these metal ions is bridged to Mn2 through μ_2-O (hydrazone) bridges (Mn−O−Mn angles in the range 127.1−130.9°). Within the basal triangle bridging connections between Mn3 and Mn4 is provided a μ_2-1,3-acetate bridge, and between Mn4 and Mn5 by a μ_2-1,3-acetate bridge. Another acetate connecting Mn3 and Mn5 is disordered over two positions (O18, O19, O20; Figure 3) with the 1,3-mode refined to 0.517(13)-occupancy, while the 1,1-mode refined to 0.483(13)-occupancy. The ellipsoids for both components are very reasonable, and so it would be difficult to assign one type of bridge as being significantly dominant. On the basis of the separation of the bridged Mn atoms it would appear that either arrangement can be accommodated. Mn−O−Mn angles at the μ-$O_{acetate}$ bridge fall in the range 92.3−92.5°. A detailed analysis of the bond lengths around each Mn center gives averages of 2.037 Å, 2.189 Å, 2.027 Å, 2.020 Å, and 2.025 Å for Mn1−Mn5 respectively (corresponding BVS[22] values 2.87, 2.03, 3.05, 3.05, 3.29 respectively) indicating that Mn2 is Mn(II) and the other Mn centers are Mn(III). This arrangement of Mn centers is the same as that reported previously for the Cs_2 complex **1**.[10]

The arrangement of the three ligands around each Mn_5 cluster creates an end pocket composed of six oxygen atoms from the three vanillin end pieces. The phenolic oxygen atoms bind terminally to Mn3, Mn4, and Mn5, leaving the OMe groups free. In **1** this arrangement provides a fortuitous group of six oxygen donors at each end of the chain, which attract and bind two Cs ions.[10] No additional cations were added in the synthesis of **2**, but surprisingly oxygen atoms (O24) show up in the two pockets instead (Figure 3), with O24−O nearest neighbor contacts in the range 2.76−2.93 Å to the six vanillin oxygen atoms and also O13. This is considered reasonable for hydrogen bonding interactions, which suggests that O24 is part of a water molecule. However, looking at the overall charge balance, based on the mixture of Mn(II) and Mn(III) centers in each Mn_5 cluster, and the reasonable assumption that each ligand loses three protons, oxygen O24 is in fact a hydronium, H_3O^+ ion.

$[Mn_{10}(L4\text{-}3H)_6(O)_2(CH_3O)_4(CH_3COO)_4(CH_3OH)_2Li_2(LiOH)_2]$-$((CH_3CH_2)_2O)_2$ (**3**). Crystallographic details for **3** are given in Table 1, and important bond distances and angles in Supporting Information, Table S2. A summary of key dimensions is given in Table 2. The structure of the basic deca-manganese cluster is essentially the same as that in **2**, and the asymmetric half unit is shown in Figure 4. The vanillin end

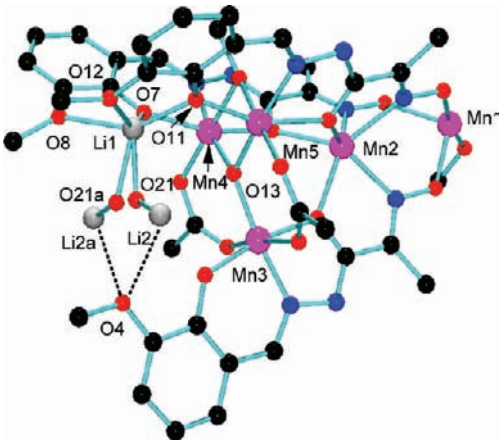

Figure 4.

pocket is home in this case to an unusual Li based cluster comprising Li1 at unit occupancy, bonded to four oxygen atoms on one side of the cavity (O7, O8, O11, O12; Li−$O_{ave.}$ 2.12 Å), with a connected, disordered LiO based component (Li2−O21−O21a−Li2a), in which each Li and O appears at half occupancy. The small Li^+ ion does not effectively fill the space within the vanillin cavity, unlike the situation with Cs^+, and the appearance of another Li site may simply be a response on the part of the alkali metal ion to make the most effective use of the oxophilic environment. A close examination of the Mn_3 triangle within the Mn_5 cluster reveals a difference in the arrangement of bridging groups compared with **2** (and also **4**−**6**; vide infra). There are two μ_2-1,3-acetate bridges and one μ_2-OMe bridge, similar to the situation observed for **1**. This seems to result from a geometric flexing of the ligand superstructure around the Mn_5Li vanillin subunit, in response to the asymmetric occupation of the vanillin cavity by the Li ion assembly. In this context it is reasonable to assume that the volume occupied by the Li_2O subunit approximates that of the Cs^+ ion (vide infra).[10]

Mn−O distances within the Mn_3-μ_3-O triangle fall in the range 1.88−1.92 Å. Other charge considerations for the remaining parts of the overall cluster are the same as for **1** and **2**, based on the same mixture of Mn(II) and Mn(III) sites (BVS values 3.10, 2.20, 3.21, 3.25, 3.30 for Mn1 to Mn5 respectively), and the methoxide bridges (Mn−O distances 1.961 Å, 1.947 Å), and so the logical conclusion is that on the reasonable basis that each ligand loses three protons, the disordered LiO subunit is likely to be LiOH, which was added during the synthesis of **3**. A proton associated with O21−O21a was not located in difference maps. The change in structure of the Mn_3-μ3-O subunit, resulting from the combination of two

dx.doi.org/10.1021/ic3003355 | Inorg. Chem. 2012, 51, 11241−11250

μ_2-1,3-acetate bridges and one μ_2-OMe bridge, leads to different dimensions within the Mn_5 cluster compared with **2** (Table 2) with a larger range of Mn−O−Mn angles at both the hydrazone and the oxide bridges.

$[Mn_{10}(L\text{-}3H)_6(O)_2(CH_3O)_2(CH_3COO)_6(CH_3OH)_2Na_2]\cdot(CH_3OH)_3(CH_3CH_2)_2O)_4$ (***4***). Crystallographic details for **4** are given in Table 1, important bond distances and angles in Supporting Information, Table S3, and a summary of key dimensions is given in Table 2. The overall structure of the deca-manganese cluster is shown in Figure 5, and is essentially identical to that in **1**−**3**,

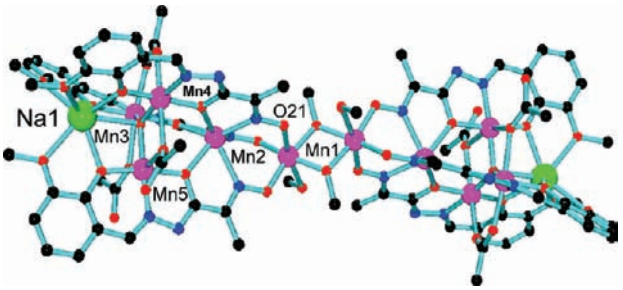

Figure 5.

with the two Mn_5 based halves bridged through two short MeO linkages (Mn1−O 1.930, 1.942 Å). In this case the vanillin cavity is occupied by a single Na^+ ion. The Mn_5Na half cluster is shown in Figure 6. Each Na^+ ion is effectively bonded to

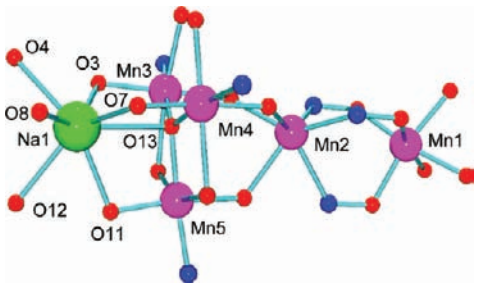

Figure 6.

seven neighboring O atoms (Na−O distances 2.37−2.67 Å), with no alkali metal disorder, and so unlike the Li^+ case the Na^+ ion seems to fit more comfortably in the vanillin cavity. It is of interest to note that the Na1−O13 distance (2.615 Å) is less than two of the Na−O distances to the OMe vanillin groups. The three acetates adopt a mixture of two μ_2-1,1 and one μ_2-1,3 bridging modes. Bond distances at the five manganese centers fall into similar ranges to those observed in **1**−**3**, with BVS values (3.15, 2.21, 3.49, 3.55, 3.42 for Mn1 to Mn5 respectively) which reflect exactly the same distribution of oxidation states (Mn(III), Mn(II), Mn(III), Mn(III), Mn(III) respectively).[22] The μ_3-O atom again is an oxide (O13−Mn distances 1.84−1.91 Å), which indicates that all the ligands have a −3 charge.

$[(L4\text{-}3H)_3Mn(III)_4Mn(II)(O)(CH_3OH)(CH_3O)(CH_3COO)_3K]_2\cdot(CH_3OH)_3(CH_3CH_2)_2O)_4$ (***5***). Crystallographic details for **5** are given in Table 1, and important bond distances and angles in Supporting Information, Table S4. A summary of key dimensions is given in Table 2. The structure of the deca-manganese cluster is shown in Figure 7, and is identical to that in **4**, with the two Mn_5 based halves bridged through two MeO linkages (Mn1−O 1.938,

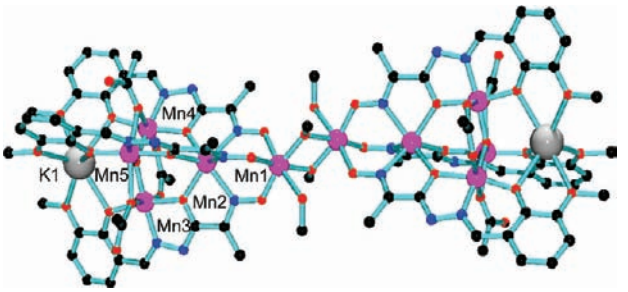

Figure 7.

1.940 Å). The vanillin O_6 end pockets in this case are occupied by two K^+ ions. Each K^+ ion is effectively bonded to six neighboring O atoms (K−O distances 2.65−2.75 Å), with no alkali metal disorder. In this case, unlike the sodium case, the K1−O13 distance (2.814 Å) is probably too long to qualify as a bond. The three acetates adopt the same mixture of two μ_2-1,1 and one μ_2-1,3 bridging modes as observed in **4**. Bond distances at the five manganese centers fall into similar ranges to those observed in **1**−**4**, with BVS values (3.23, 2.30, 3.38, 3.41, 3.30 for Mn1 to Mn5 respectively) which reflect exactly the same distribution of oxidation states (Mn(III), Mn(II), Mn(III), Mn(III), Mn(III), respectively).[22] The μ_3-O atom again is an oxide (O13−Mn distances 1.87−1.90 Å), which indicates that all the ligands have a −3 charge.

$[(L4\text{-}3H)_3Mn(III)_4Mn(II)(O)(CH_3OH)(CH_3O)(CH_3COO)_3Rb]_2\cdot(H_2O)_{15}$ (***6***). Crystallographic details for **6** are given in Table 1, and important bond distances and angles in Supporting Information, Table S5. A summary of key dimensions is given in Table 2. The structure of the deca-manganese cluster is shown in Figure 8, and the half cluster in Figure 9. The basic Mn_{10} double

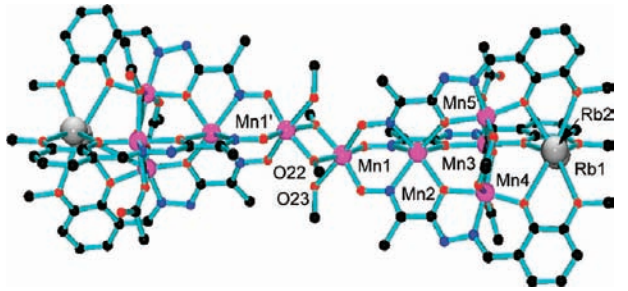

Figure 8.

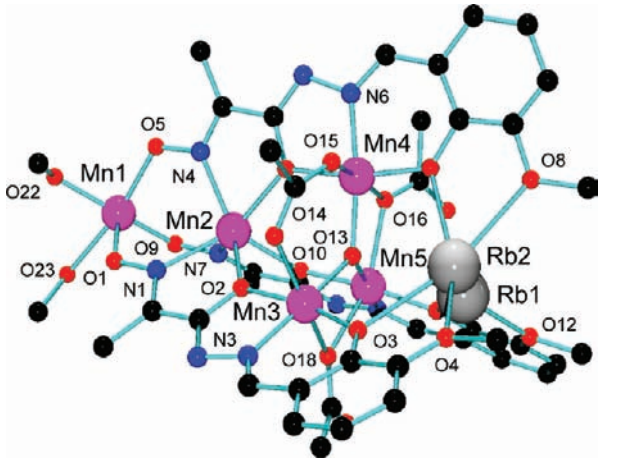

Figure 9.

dx.doi.org/10.1021/ic3003355 | *Inorg. Chem.* 2012, 51, 11241−11250

cluster motif is repeated in **6**, but each vanillin end pocket is occupied by two disordered Rb^+ ions (unit total occupancy). Three acetates bind to the Mn_3 triangle, with a mixture of two μ_2-1,1 and μ_2-1,3 bridging modes. Bond distances at the five manganese centers fall into similar ranges to those observed previously, with BVS values (3.01, 2.25, 3.18, 3.19, 3.10 for Mn1 to Mn5, respectively) which reflect exactly the same distribution of oxidation states (Mn(III), Mn(II), Mn(III), Mn(III), Mn(III), respectively).[22] The overall charge balance sensibly assumes that each ligand bears a −3 charge, and that each Rb site corresponds to +1 charge overall. The incorporation of two Rb(I) ions parallels the previous situations, but it is surprising that two disordered Rb atoms are present at each oxophilic O_6 site. This implies that the Rb ions are not restricted to a fixed coordination position within the cavity, implying a slight mismatch in terms of the Rb ion size and the cavity. This is unexpected given the larger size of Rb^+ compared with Na^+ and K^+, and the fact that these ions did not show disorder. In the Cs^+ case the larger size of this ion clearly allows it to fit the pocket more comfortably. The longer contacts to the μ_3-O13 bridge (2.949 Å, 3.053 Å) are considered too long to be bonds and so each Rb^+ ion is considered to be six-coordinate.

Within the series of complexes involving H_3O^+ and the alkali metal ions in the vanillin pockets there is a general trend in the relationship of the size of the guest and the way in which it interacts with the oxygen rich environment present. The alkali metal ions increase in size as a function of descending position in the Periodic Table (Li^+ 90, Na^+ 116, K^+ 152, Rb^+ 166, Cs^+ 181 pm), and with the exception of Li and Rb all fit comfortably without disorder. However, the proximity of the guest ion to O13 gradually increases from Na to Cs implying that the alkali metal ion is moving further away from the Mn_5 cluster subunit. With Li the alkali metal Li1 is bonded tightly to four oxygen atoms in the cavity (vide supra), but all metal ions in the Li cluster are well separated from O13. This is clearly a function of the small Li^+ radius. The general dimensions of the Mn_5 cluster subunit are similar within the series, but there is a significant difference in the Li case (vide supra). The Mn_3-μ_3-O triangle has the most pyramidal distortion, and the Mn−$O_{hydrazone}$−Mn angles span the largest range (Table 2).

Magnetic Properties. All of the complexes **2**−**6** have the same double Mn_5 cluster structure with the same arrangement of Mn(II) and Mn(III) centers within each Mn_5 half, and comparable dimensions involving all bridging groups (Table 2). This is quite remarkable, but confirms the primary nature of the ligand L4 in directing the cluster assembly under what are similar preparative conditions in all cases. From the perspective of exchange coupling within each Mn_5 cluster subunit the bridging oxygen atoms will define the spin exchange model. Mn2 is connected to Mn3−Mn5 by μ-$O_{hydrazone}$ bridges with Mn−O−Mn angles in the range 125.5 −132.0°, while within the basal triangle for **2**, and **4**−**6** two single atom oxygen bridges from two μ_2-1,1-acetates exist with Mn−O−Mn angles in the range 88.7°−94.0°. In the case of **3** the single Mn−O_{OMe}−Mn angle is 94.8°. The three basal Mn(III) centers form a triangle around O13 in all cases, with Mn−O−Mn angles in the range 99.3−128.4°. The solid angle sums are close to 360°, indicating slight pyramidal distortion of the O group from the least-squares triangular basal plane toward the vanillin pocket. All of these connections would be expected to propagate antiferromagnetic exchange. The group of three oxime bridges adopts the normal NO bridging mode, which should lead to relatively strong antiferromagnetic exchange, and the methoxide bridges connecting each Mn_5 hall would also be expected to lead to antiferromagnetic exchange (vide infra).

The magnetic properties of **1** have already been reported,[10] and characteristic features of the variable temperature magnetic data include a distinct maximum in χ_{mol} at ∼20 K, and a moment dropping from 14.6 μ_B at 300 K to 2.14 μ_B at 2 K, indicative of significant intramolecular antiferromagnetic coupling throughout the whole cluster. The exchange was modeled on the basis of two antiferromagnetic Mn_5 clusters (ground state S = 3/2 in the antiferromagnetic limit), coupled together through an additional antiferromagnetic interaction via the methoxide bridges, which would effectively lead to an S = 0 ground state. Variable temperature magnetic data for **2** are shown in Figure 10 as plots of susceptibility (χ) and moment

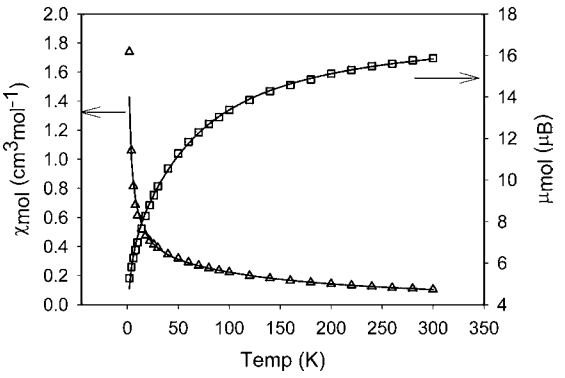

Figure 10.

(μ) expressed per mole. No maximum is observed in χ, even at low temperature, unlike the situation in **1**, but the smooth drop in moment on lowering the temperature from 15.87 μ_B at 300 K to 5.28 μ_B at 2 K, indicates the presence of dominant intramolecular antiferromagnetic exchange. The room temperature moment of 15.87 μ_B is consistent with the presence of eight high spin Mn(III) and two high spin Mn(II) centers, but the value of 5.28 μ_B at 2 K is much higher than observed for **1**, and suggests a nonzero ground state spin. In fact it is close to the expected value for a species with two effectively isolated S_T = 3/2 centers in the ground state (Curie value 5.50 μ_B), suggesting only weak antiferromagnetic exchange between the two halves. Magnetization data per mole as a function of field at 2 K (Supporting Information, Figure S1) do not show saturation, and M values rise steadily to 5.8 Nβ at 5.0 T, again approximating a system composed of two halves each with a spin of 3/2.

Dealing with a spin exchange model for such a large 42 electron cluster presents a significant challenge, because of the enormous dimensions of the matrices involved, and would be beyond the capabilities of the average computer. As an illustration of the large nature of the spin vector summation calculation, for a full cluster model with each high spin Mn(III) site (S = 4/2) substituted by a smaller S = 2/2 site (total of 26 electrons), and assuming that each adjacent pair of metal ions is coupled, there are 27386 spin states, with the largest matrix dimension of 4788. Increasing the spin content to 4/2 for each Mn(III) center would lead to an enormous calculation, and so a simplified approximation was adopted. This was achieved by considering just one-half of the molecule, and modeling the possible coupling between each half using a Weiss (θ) correction. This leads to a sensible assessment of the intramolecular exchange within each Mn_5 half, which would

dx.doi.org/10.1021/ic3003355 | Inorg. Chem. 2012, 51, 11241−11250

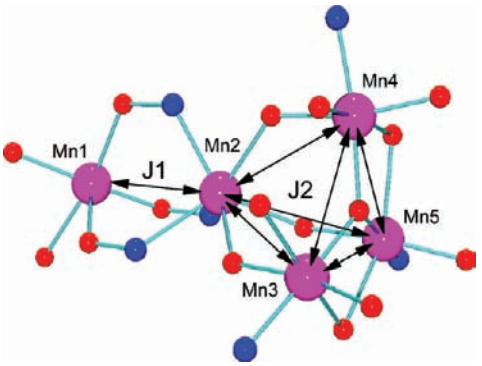

Figure 11.

be mirrored in the second half of the molecule. Figure 11 shows the spin exchange coupling routes within each half Mn_5 cluster subunit, assuming all adjacent connections contribute. However, to avoid overparameterization and given the general similarity of the Mn−O−Mn oxygen bridge angles within the Mn_4 part of this cluster, a simplification was adopted by assuming that all intermanganese couplings are approximately the same. The NO bridging connections are, however, expected to lead to somewhat larger exchange, and as a consequence are included as a different exchange component. These are highlighted as J1 (μ-NO) and J2 (μ-Mn_4) (Figure 11). Equation 1 shows an appropriate exchange Hamiltonian. There are 433 spin states associated with the Heisenberg spin-only exchange calculation resulting from this expression. Data fitting was carried out within the framework of the software package MAGMUN4.1[23] which generates the spin states and their relative energies from the spin vector summation, and substitutes them directly into the Van Vleck eq 2.

$$H_{ex} = -J1\{S_1 \cdot S_2\} - J2\{S_2 \cdot S_3 + S_2 \cdot S_4 + S_2 \cdot S_5 + S_3 \cdot S_4 + S_3 \cdot S_5 + S_4 \cdot S_5\} \quad (1)$$

$$\chi_M = \frac{N\beta^2 g^2}{3k(T-\theta)} \frac{\sum S'(S'+1)(2S'+1)e^{-E(S_i)/kT}}{\sum (2S'+1)e^{-E(S_i)/kT}} + \mathrm{TIP} \quad (2)$$

A good fit for compound **2** was obtained for g = 2.143(8), J1 = −10.6(1) cm^{-1}, J2 = −5.3 cm^{-1}, TIP (temperature independent paramagnetism) = 400 × 10^{-6} cm^3 mol^{-1}, θ = −1 K, 10^2R = 1.2 ($R = [\sum(\chi_{obs} - \chi_{calc})^2/\sum\chi_{obs}^2]^{1/2}$). The solid lines in Figure 10 were calculated using these parameters. The averaged exchange situation within the Mn_4 subunit is sensible given the range of angles associated with the oxygen bridges, and the larger value of J1 associated with the triple NO bridge connection between Mn1 and Mn2 is reasonable. The small negative θ correction can be interpreted in terms of a very weak antiferromagnetic exchange term between both halves of the overall structure, which is perhaps unexpected given the OMe connections (vide infra). The exchange integrals are consistent with the analysis of the Cs derivative (**1**), except that in this case all exchange pathways were considered to be the same ($J_{av.}$ = −6.3 cm^{-1}).[10]

One feature which distinguishes the magnetic profile of **2** from that of the Cs derivative **1** concerns the presence of a distinct maximum in χ_{mol} at 20 K in **1**, which is absent in **2**. Also the moment for **1** at 2 K is 2.14 μ_B, which clearly points to a significant difference between the two compounds in relation to coupling between the two halves of the molecule, and that in **1** the exchange is much stronger. In this case modeling the low temperature region (<30 K) accurately was not possible, and so only the data above 30 K were fitted to eq 1 (J1 = J2). A large negative θ value (−10 K) was required for a good fit, and while it does not have any real meaning in the sense of the normally expected weak longer range exchange effects, it does suggest that coupling between the two Mn_5 halves is quite significant, as might have been expected.[10]

Variable temperature magnetic data for **3** (Li) show a generally similar overall profile to that observed for **2**, but a slight shoulder occurs in the χ versus temperature plot at ∼20 K (Supporting Information, Figure S2), at a similar temperature to the maximum in χ observed for **1**. The moment drops smoothly on lowering the temperature from 14.7 μ_B at 300 K to 2.74 μ_B at 2.0 K, indicating the presence of intramolecular antiferromagnetic exchange, but the value at 2 K is much lower than that observed for **2**, and although it approaches the value observed for **1**, it is significantly higher. This suggests that while the dominant exchange effects are associated with the Mn_5 cluster subunits, there must again be a significant coupling between each Mn_5 half, and also suggests some influence on the overall intramolecular exchange situation by the species occupying the vanillin cavities.

Data fitting for **3** was attempted with eq 1, initially using all points down to 2 K, but it quickly became apparent that while fitting of the higher temperature data was possible, the data below ∼30 K could not be modeled, similar to the situation for **1**. The clear appearance of a low temperature shoulder indicates that a specific antiferromagnetic component is having a significant influence on the coupling around 20 K, and reasonably it is associated with the exchange between the two halves of the cluster via the methoxide bridges (vide supra). This being the case, the data above 30 K were treated separately (Figure 12), assuming

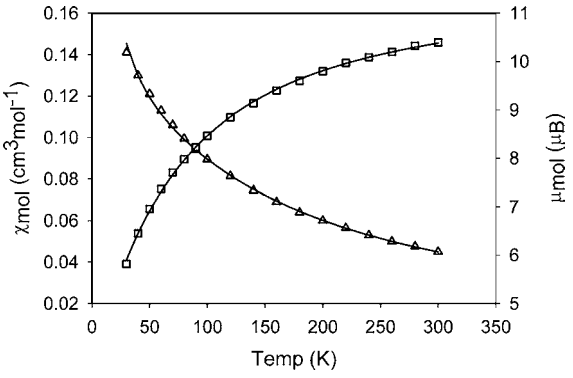

Figure 12.

that in this temperature region the coupling within the Mn_5 subunits would dominate the exchange properties. A good fit was obtained for g = 2.047(5), J1 = −13.1(1) cm^{-1}, J2 = −6.4(1) cm^{-1}, θ = −4 K (10^2R = 0.62) in reasonable agreement with **1** and **2** (see Figure 12 for fitted curve). The large Weiss correction term clearly points to the fact that the overall model does not account appropriately for the low temperature region, and that the two Mn_5 halves must undergo spin coupling.

Since there is no reason to expect any other exchange situation, given the nature of the bridges, and since the divergence of the model occurs only at low temperatures, for example, below 30 K, one possible approach to modeling the maximum in χ in the low temperature region would be to consider each Mn_5 subunit as a

dx.doi.org/10.1021/ic3003355 | Inorg. Chem. 2012, 51, 11241−11250

ferrimagnetic cluster in its own right with an $S = 3/2$ ground state in the low temperature limit, resulting from the noncompensation of the spin summation in the cluster through antiferromagnetic exchange. Using a simple dinuclear $S = 3/2$ model as a test case a maximum in χ can be generated at ~20 K, matching the features in **1** and **3**, using a J value of -10 cm^{-1}. Although the absolute χ values do not agree, as would be expected, the fact that a maximum can be generated at a corresponding temperature points to the importance of coupling between the two Mn_5 halves, and that a substantial θ correction would of necessity be required to try to take it into account (vide supra). However, the use of such large θ values is really not a meaningful approach, but what is important in the context of the model is the temperature at which the maximum occurs, which is a direct measure of the exchange between each Mn_5 half regardless of the magnitude of the susceptibility itself. Within the constraints of the current modeling approach assigning an exact exchange component to the methoxide bridges is not possible.

Other members in the alkali metal series $Mn_{10}M_2$ (**4**–**6**), where M = Na^+, K^+, Rb^+, respectively, have variable temperature magnetic profiles which are all very similar to those of **1** and **3**, with moments dropping smoothly from ~15 μ_B at 300 K to <2.5 μ_B at 2 K, and similar maxima in χ_{mol} at ~20 K . Attempts to model the variable temperature data were again limited to the temperature region above 30 K, but J and θ values were similar to those observed for **1** and **3**, as would be expected. However, there is an interesting trend in the low temperature (2 K) magnetic moment values (M (μ_B) = H_3O^+ (5.28), Li^+ (2.74), Na^+ (2.43), K^+ (2.16), Rb^+ (2.48), Cs^+ (2.14)), which is clearly a reflection on the interaction between the two Mn_5 halves via the methoxide bridges (vide supra). In the case of M = H_3O^+ (**2**) the relatively high moment points to a very weak interaction between each Mn_5 subunit, which is corroborated by a good data fit over the entire 2–300 K temperature range, and a very small corrective θ term, while for Cs^+ the very low value signifies a substantial antiferromagnetic interaction via the methoxide bridges. Barring a slight anomaly with Rb^+ a sensible explanation can be offered to explain the trend. Metal ions inherently have a property of polarization based on their ionic potential values (q/r, charge/radius ratio), a feature of paramount importance in biology where migration of ions through membrane channels is controlled by electronic and electrostatic potentials, and also such effects can control enzyme catalyzed reactions through polarization effects on coordinated functional groups. In the alkali metal series one would anticipate that this polarization trend would be $Li^+ > Na^+ > K^+ > Rb^+ > Cs^+$ based on ionic size.

The unusually high moment in **2** means that the inclusion of H_3O^+, hydrogen bonded within the vanillin pocket, creates a quite significant polarizing effect on the electron density in each Mn_5 subunit, to the extent that it is effectively constrained to remain almost exclusively within the cluster itself, and subject mostly to intracluster exchange. Charge delocalization into the methoxide bridges is minimal. Turning to the alkali metals, the Li^+ ion would be expected to create the strongest electron polarization effect, with a gradual weakening toward Cs^+ as size increases (vide supra). The clear trend in moments at 2 K reflects this, with Li^+ exerting the strongest effect, in the sense that some electron density within each Mn5 cluster effectively leaks through the methoxide bridges. As the polarization effect diminishes, the moment drops because of more and more charge delocalization via methoxide coupling. The slight anomaly with the Rb^+ complex is unexpected, but may be associated with the disorder at the alkali metal site. However, the overall trend indicates that while the alkali metal ions are influencing exchange between each half cluster via the OMe bridges slightly, based on their polarizing effects, surprisingly it is weak in comparison with H_3O^+.

Scanning Tunnelling Microscopy (STM) and Current Imaging Tunnelling Spectroscopy (CITS). The structural and electronic properties of complex **1** have been investigated by Scanning Tunneling Spectroscopy (STM) and Current Imaging Tunneling Spectroscopy (CITS) techniques. STM allows the imaging a single molecule on surfaces,[24] while CITS allows the probing of the electronic states of the molecules as a function of energy within a range of few eV around the Fermi level.[25,26] **1** was deposited on an HOPG surface and subsequently studied by STM/CITS techniques. Application of complex **1** to HOPG surfaces reveals a wealth of organized single molecular patterns at the surface step-edges. Typical low- and high-resolution STM images of the Mn complex on HOPG are shown in Figure 13, starting with a single molecular line

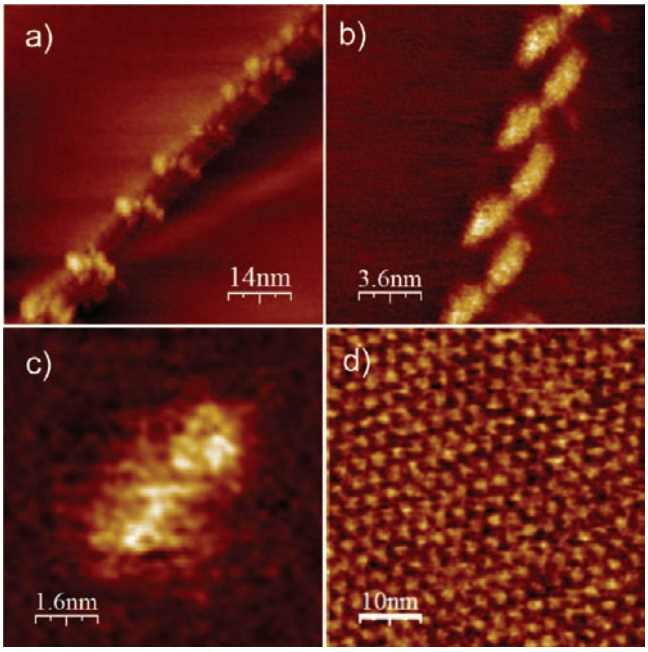

Figure 13. STM results of complex **1** deposited onto a HOPG surface: (a) Large scale image showing single molecules hanging on next to the HOPG step; (b) Zigzag line of single molecules well organized at the defects of HOPG; (c) An isolated single molecule and (d) STM topography of a monolayer of $Mn_{10}Cs_2$.

(Figure 13a), zigzag patterns of single molecules (Figure 13b), an isolated single molecule (Figure 13c), as well as a monolayer assembly (13d). The dimensions of the individual spot obtained from Figure 13c is around 3.1 nm × 1.5 nm, which matches the dimensions of a single molecule of (approx. 2.8 nm × 1.2 nm) obtained from X-ray crystallographic data.

To understand the local electronic structure of complex **1** (Figure 14a), energy-resolved I–V spectra (CITS) at the single molecule level were carried out. Figure 14b shows a constant current topography image, together with a simultaneously measured CITS current image (Figure 14c), which shows the spatial distribution of the tunneling current at −0.8 V. Obviously the topographic image presents a diffuse representation of the shape of the molecule,[26] but the dimensions of the feature in Figure 14b again conform to the dimensions of a single molecule obtained from X-ray data of complex **1**. It is

dx.doi.org/10.1021/ic3003355 | Inorg. Chem. 2012, 51, 11241–11250

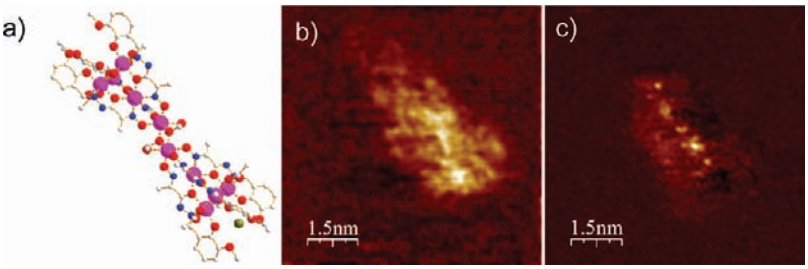

Figure 14. (a) Orientation of a single $Mn_{10}Cs_2$ complex. (b, c) Simultaneously recorded topography (panel b) and CITS current image at −0.8 V (panel c) from a single scan. Tip stabilization parameters were V = −0.1 V and I = 30 pA.

only possible to extract information about the overall topography of the molecule, as is expected.[3,27] In contrast to this topographic imaging, the CITS current map shows some bright points which represent molecular regions of high tunneling current probability (Figure 14c). The supramolecular cluster contains 10 Mn ions, and two Cs ions, but they are not all in the same plane and the neighboring distances of the Mn ions are very small. Therefore it is difficult to resolve them clearly in the CITS image. By considering that the maximum contribution to the local density of states close to the Fermi level will be found at the metal centers,[3,27] the intense spots can be ascribed to the positions of the Mn and Cs ions in complex **1**. A high contrast at negative bias voltages shows that tunneling does occur into occupied states of **1**. Therefore, Figure 14c can be considered as a map of the highest occupied molecular orbitals (HOMOs) of complex **1**. At a positive bias voltage there was little contrast, and the features are not well represented. The image is not presented here. It is clearly seen from Figure 14c that all bright spots do not show the same contrast. This is expected because the Mn centers in complex **1** are at different oxidation states, and the Cs ions are different metal ions. It is of significance to note that the end spots appear to be slightly larger and brighter than the other spots, consistent with their assignment as Cs^+ ions. In this context it is significant to note that these two spots are separated by ∼28 Å, based on the rather crude scale dimension, and the separation of the Cs ions according to the X-ray structure, is 23.6 Å, which is a reasonable comparison.

CONCLUSIONS

The incorporation of different coordinating groups into a hydrazone based polytopic ligand tests the idea that based on individual group complexation behavior it is possible that collectively the combined effect could create an assembled structure where these elements act in concert, but also in a sense individually, to generate a possibly predictable outcome. In the case of the Mn_{10} based assemblies the hydrazone oxygen atoms fulfill their expected μ-O bridging role by creating the Mn_4 portion of the Mn_5 cluster. The resulting trigonal arrangement of the three ligands involved presents the three oxime NO groups favorably to bind to the fifth Mn center, and also the fortuitous resulting arrangement of the three vanillin subunits leads to the formation of the "oxophilic" O_6 pocket, which attracts the alkali metal ions and a hydronium ion. This situation has also been observed recently with a vanillin based ligand built on 3-amino-1,2-propanediol backbone,[28] which forms a mixed oxidation state Mn_4 cluster with Ca(II) incorporated in a similar O_6 based cavity. The unusual mixture of Mn oxidation states is completely reproducible regardless of the nature of the alkali metal or its absence, and rests with the influence of the ligands, the particular disposition of the metal centers, and the associated bridging groups. The most reasonable explanation for the presence of Mn(III) is through aerial oxidation, since air was not excluded during synthesis.

Magnetic exchange in the Mn_{10} assemblies is dominated by antiferromagnetic behavior, with coupling nominally extending throughout the whole polymetallic cluster. However, depending on the guest in the vanillin pockets, the inter Mn_5 subunit exchange is modulated by the polarizing properties of the guest itself, with H_3O^+ exerting the strongest effect. This unique observation suggests that the overall exchange situation can be adjusted, and the coupling between each Mn_5 half almost "switched off" by the simple expedient of applying a controlled electrostatic effect in one part of the cluster, in this case the vanillin end pockets. Surface studies show that the Cs complex **1** can be deposited on HOPG, with molecular definition of individual molecules based on the metal centers through CITS imaging. Further studies on the general nature of the assembly of the $Mn_{10}M_2$ system with other oxophilic metal cations are in progress, and preliminary results indicate that dipositive, for example, Ba(II), and tripositive, for example, Gd(III,) ions can also be incorporated, and that in the Gd(III) case exchange extends to include the Gd(III) ion as well.[29]

ASSOCIATED CONTENT

Supporting Information

Further details are given in Figures S1−S2 and Tables S1−S5. This material is available free of charge via the Internet at http://pubs.acs.org.

AUTHOR INFORMATION

Corresponding Author

*E-mail: lk.thompson@mun.ca.

Notes

The authors declare no competing financial interest.

ACKNOWLEDGMENTS

We thank NSERC (Canada) for financial support for these studies (L.K.T., MM). M.S.A. thanks Prof. P. Müller for the donation of STM equipment.

REFERENCES

(1) Dawe, L. N.; Shuvaev, K. V.; Thompson, L. K. *Chem. Soc. Rev.* **2009**, *38*, 2334 , and references therein.

(2) Dawe, L. N.; Abedin, T. S. M.; Thompson, L. K. *Dalton Trans.* **2008**, 1661.

(3) Dey, S. K.; Abedin, T. S. M.; Dawe, L. N.; Tandon, S. S.; Collins, J. L.; Thompson, L. K.; Postnikov, A. V.; Alam, M. S.; Müller, P. *Inorg. Chem.* **2007**, *46*, 7767.

(4) Anwar, M. U.; Thompson, L. K.; Dawe, L. N. *Dalton Trans.* **2011**, *40*, 1437.
(5) Tang, J.; Hewitt, I. J.; Madhu, N. T.; Chastanet, G.; Wernsdorfer, W.; Anson, C. E.; Benelli, C.; Sessoli, R.; Powell, A. K. *Angew. Chem., Int. Ed.* **2006**, *45*, 1729.
(6) Hewitt, I. J.; Tang, J.; Madhu, N. T.; Anson, C. E.; Lan, Y.; Luzon, J.; Etienne, M.; Sessoli, R.; Powell, A. K. *Angew. Chem., Int. Ed.* **2010**, *49*, 6352.
(7) Sessoli, R.; Powell, A. K. *Coord. Chem. Rev.* **2009**, *253*, 2328.
(8) Lin, P.-H.; Burchell, T. J.; Ungur, L.; Chibotaru, L. F.; Wernsdorfer, W.; Murugesu, M. *Angew. Chem., Int. Ed.* **2009**, *48*, 9489.
(9) Long, J.; Habibi, F.; Lin, P.-H.; Korobkov, I.; Enright, G.; Ungur, L.; Wernsdorfer, W.; Chibotaru, L.; Murugesu, M. *J. Am. Chem. Soc.* **2011**, *133*, 5319.
(10) Anwar, M. U.; Dawe, L. N.; Thompson, L. K. *Dalton Trans.* **2011**, *40*, 8079.
(11) *SHELX97*: Sheldrick, G. M. *Acta Crystallogr.* **2008**, *A64*, 112.
(12) *DIRDIF99*: Beurskens, P. T.; Admiraal, G.; Beurskens, G.; Bosman, W. P.; de Gelder, R.; Israel, R.; Smits, J. M. M. The DIRDIF-99 program system, Technical Report of the Crystallography Laboratory; University of Nijmegen: Nijmegen, The Netherlands, 1999.
(13) Cromer, D. T.; Waber, J. T. In *International Tables for X-ray Crystallography* ; The Kynoch Press: Birmingham, England, 1974; Vol. *IV*, Table 2.2 A.
(14) Ibers, J. A.; Hamilton, W. C. *Acta Crystallogr.* **1964**, *17*, 781.
(15) Creagh, D. C.; McAuley, W. J. In *International Tables for X-ray Crystallography*; Wilson, A.J.C., Ed.; Kluwer Academic Publishers: Boston, MA, 1992; Vol *C*, Table 4.2.6.8, pp 219−222.
(16) Creagh, D. C.; Hubbell, J. H. In *International Tables for X-ray Crystallography*; Wilson, A.J.C., Ed.; Kluwer Academic Publishers: Boston, MA, 1992; Vol *C*, Table 4.2.4.3, pp 200−206.
(17) *CrystalStructure 3.7.0: Crystal Structure Analysis Package*; Rigaku and Rigaku/MSC: The Woodlands, TX, 2000−2005.
(18) Watkin, D. J.; Prout, C. K.; Carruthers, J. R.; Betteridge, P. W. *CRYSTALS*, Issue 10; Chemical Crystallography Laboratory: Oxford, U.K., 1996.
(19) Spek, A. L. *J. Appl. Crystallogr.* **2003**, *36*, 7.
(20) Hamers, R. J.; Tromp, R. M.; Demuth, J. E. *Phys. Rev. Lett.* **1986**, *56*, 1974.
(21) Horcas, I.; Fernandez, R.; Gomez-Rodriguez, J. M.; Colchero, J.; Gomez-Herrero, J.; Baro, A. M. *Rev. Sci. Instrum.* **2007**, *78*, 013705.
(22) (a) Palenik, G. J. *Inorg. Chem.* **1997**, *36*, 122. (b) O'Keeffe, M.; Brese, N. E. *J. Am. Chem. Soc.* **1991**, *113*, 3226.
(23) MAGMUN4.1/OW01.exe is available from the authors (http://www.ucs.mun.ca/∼lthomp/magmun). It was developed by Dr. Zhiqiang Xu, and OW01.exe by Dr. O. Waldmann. Source codes are not distributed. The origin of the programs should be quoted.
(24) (a) Binnig, G.; Rohrer, H.; Gerber, C.; Weibel, E. *Appl. Phys. Lett.* **1982**, *40*, 178. (b) Tersoff, J.; Hamann, D. R. *Phys. Rev. B* **1985**, *31*, 805.
(25) Stroscio, J. A.; Kaiser, W. J., Eds.; *Scanning Tunneling Microscopy*; Academic Press: New York, 1993.
(26) Alam, M. S.; Dremov, V.; Müller, P.; Mal, S. S.; Hussain, F.; Kortz, U. *Inorg. Chem.* **2006**, *45*, 2866.
(27) (a) Petukhov, K.; Alam, M. S.; Rupp, H.; Müller, P.; Thompson, L. K.; Ruben, M.; Saalfrank, R. W.; Lehn, J.-M. *Coord. Chem. Rev.* **2009**, *253*, 2387. (b) Ruben, M.; Lehn, J.-M.; Müller, P. *Chem. Soc. Rev.* **2006**, *35*, 1056. (c) Saalfrank, R. W.; Scheurer, A.; Bernt, I.; Heinemann, F. W.; Postnikov, A. V.; Schünemann, V.; Trautwein, A. X.; Alam, M. S.; Rupp, H.; Müller, P. *Dalton Trans.* **2006**, 2865. (d) Alam, M. S.; Strömsdörfer, S.; Dremov, V.; Müller, P.; Kortus, J.; Ruben, M.; Lehn, J.-M. *Angew. Chem., Int. Ed.* **2005**, *44*, 7896.
(28) (a) Hewitt, I. J.; Tang, J.-K.; Madhu, N. T.; Clérac; Buth, G.; Anson, C. R.; Powell, A. K. *Chem. Commun.* **2006**, 2650. (b) Nayek, S.; Nakek, H. P.; Dehnen, S.; Powell, A. K.; Reedijk, J. *Dalton Trans.* **2011**, *40*, 2699.
(29) Anwar, M. U.; Dawe, L. N.; Thompson, L. K., unpublished results.